Quarterly Journal of the
Royal Meteorological Society

RMetS

Extreme precipitation events over northern Italy. Part II: Dynamical precursors

Federico Grazzini[1,2] | Georgios Fragkoulidis[3] | Franziska Teubler[3] | Volkmar Wirth[3] | George C. Craig[1]

[1]Ludwig-Maximilians-Universität, Meteorologisches Institut, Munich, Germany

[2]ARPAE-SIMC, Regione Emilia-Romagna, Bologna, Italy

[3]Institute for Atmospheric Physics, Johannes Gutenberg University Mainz, Mainz, Germany

Correspondence
Federico Grazzini, Ludwig-Maximilians-Universität, Meteorologisches Institut, Theresienstrasse 37, 80333 München, Germany.
Email: federico.grazzini@lmu.de

Abstract

The connection between weather extremes and Rossby wave packets (RWP) has been increasingly documented in recent years. RWP propagation and characteristics can modulate the midlatitude weather, setting the scene for temperature and precipitation extremes and controlling the geographical area affected. Several studies on extreme precipitation events (EPEs) in the Alpine area reported, as the main triggering factor, a meridionally elongated upper-level trough as part of an incoming Rossby wave packet. In this work, we investigate a wide number of EPEs occurring between 1979 and 2015 in northern-central Italy. The EPEs are subdivided into three categories (Cat1, Cat2, Cat3) according to thermodynamic conditions over the affected region. It is found that the three categories differ not only in terms of the local meteorological conditions, but also in terms of the evolution and properties of precursor RWPs. These differences cannot be solely explained by the apparent seasonality of the flow; therefore, the relevant physical processes in the RWP propagation of each case are further investigated. In particular, we show that RWPs associated with the strongest EPEs, namely the ones falling in Cat2, undergo a substantial amplification over the western North Atlantic due to anomalous ridge-building 2 days before the event; arguably due to diabatic heating sources. This type of development induces a downstream trough which is highly effective in focusing water vapour transport toward the main orographic barriers of northern-central Italy and favouring the occurrence of EPEs.

KEYWORDS

atmospheric rivers, extreme precipitation, integrated water vapour transport, large-scale forcing, potential vorticity, Rossby wave packets

1 | INTRODUCTION

Extreme precipitation events (EPEs) in the south-Alpine area are often followed by destructive flooding with severe socio-economic impacts. This constitutes a recurring threat for the exposed population, and research efforts need to focus on a better understanding of the physical processes leading to such events. Moreover, positive trends in

extreme precipitation in this area emerge, particularly in autumn (Isotta *et al.*, 2014; Brönnimann *et al.*, 2018; Pavan *et al.*, 2019), and EPE-related fatalities increase, specifically in the subalpine regions of southern France and Italy (Petrucci *et al.*, 2019).

Many studies have investigated the dynamics of such individual events, while fewer tried to find an association between the evolution of large-scale dynamical features and EPEs on the Alpine area based on a large sample of dates (say >100 cases, see for example Martius *et al.*, 2006a; Grazzini, 2007; Pinto *et al.*, 2013; Pohorsky *et al.*, 2019). Nevertheless, the linkage between extreme precipitation in the Alpine area and the presence of a large-amplitude wave or potential vorticity (PV) streamer over western Europe is well established. For example, Martius *et al.* (2008) have indicated that 73% of days with extreme precipitation over the Swiss Alps are associated with a PV streamer.

The connection between extreme weather events and Rossby wave packets (RWPs) has been documented by many studies that examined the physical linkage between the upper-tropospheric circulation and anomalous weather at the surface. In particular, these events are often associated with pronounced undulations in the upper-tropospheric jet that typically take the form of an eastward-propagating RWP. A comprehensive list of studies investigating the role of RWPs for a variety of meteorological extremes can be found in section 7 of the recent review by Wirth *et al.* (2018). Previous studies have also suggested that EPEs are modulated by large-scale waviness associated with eastward-propagating wave packets. High RWP amplitudes over the North Atlantic and Europe imply that a succession of high-amplitude troughs and ridges may be associated with heat and moisture fluxes that create favourable conditions for the occurrence of EPEs (Piaget *et al.*, 2015; Liu *et al.*, 2020). In addition, Boers *et al.* (2019) have recently suggested that EPEs occurring at distant places (>2,500 km) are not entirely independent, since they are typically associated with the same Rossby wave packet.

Based on the above, a better understanding of the dynamical linkage between RWPs and EPEs is extremely important in evaluating, among other things, the variability of these events at climate time-scales and their predictability at weather time-scales. However, the evolution of individual RWPs may differ in several aspects, including the processes that dominate their evolution and the kind of wave breaking at their leading edge, which can eventually determine the precipitation amount and impact. Moore *et al.* (2019) point out that different types of wave breaking produce different responses in the intensity and area extension of EPEs over the USA. More relevant for the present study, they also note that cyclonic wave breaking over the eastern USA produces stronger ridge amplification downstream, over the Atlantic, due to strong PV gradient tilting and strong ascent.

Apart from the presence of a large-scale dynamical forcing factor, Sodemann and Zubler (2010) showed that moisture sources for EPEs in the Alpine area can be distant and pointed to the fact that moisture uptake in the Mediterranean is not the only source. They also highlighted the case-to-case variability in this respect. Very often large amounts of moisture come from different sectors of the Atlantic basin, with a different partition for each precipitation type, that is, stratiform or deeply convective (Winschall *et al.*, 2014). Therefore, it is important to appropriately consider the variability in dynamical forcing and moisture transport between the events in order to identify the driving factors.

According to Pohorsky *et al.* (2019), strong ridge amplification over the Atlantic appears to be a necessary prerequisite for EPEs over Europe. They show that ridge building could be further enhanced by strong diabatic heating disturbances, like those induced by recurving tropical cyclones (TCs) or associated with strong warm conveyor belts (WCBs). They recognized two main evolution patterns: in the first one, which they call "atmospheric river-like", the building of the Atlantic ridge occurs more in the zonal direction and there is a direct transport of water vapour from west to east Atlantic along the northern side of the ridge. In the second one, called the "downstream development" pathway, the water vapour flux is more meridional, associated with a greater meridional amplification of the Atlantic ridge and downstream trough. The water vapour fluxes over Europe are coming more from the southerly direction and from the northerly flow on the back of the trough. Large-scale dynamics evolution thus influences atmospheric river landfall location and subsequent precipitation extremes in Europe (Pasquier *et al.*, 2019).

The above considerations suggest that large-scale dynamical features influence the frequency and intensity of EPEs and a deeper investigation of their dynamical pathways will be essential in improving our understanding of such events. Based on the EPE categorization presented in Part I of this study (Grazzini *et al.*, 2020a), we will address the question of whether EPEs of different categories are associated with distinct large-scale dynamical evolutions.

The article is organized as follows. In Section 2, we describe the data used and the methods employed in this study. In Section 3, we present the main characteristics and synoptic conditions of the three EPE categories and examine their linkage to upper-tropospheric waviness. In Section 4, we investigate the spatio-temporal evolution of the upper-tropospheric flow and associated moisture transport prior to the EPEs and examine the dynamical processes involved based on a PV tendency framework.

Finally, the conclusions of the study are presented in Section 5.

2 | DATA AND METHODS

The atmospheric fields used in this study are retrieved from the ERA5 reanalysis (Hersbach *et al.*, 2020) over the period 1979–2015, while precipitation data, upon which the EPE definition is based, are retrieved from the gridded dataset (5 × 5 km) of the Archivo Climatologico per l'Italia centro-Settentrionale (climatological archive for central-northern Italy, ArCIS) archive (Pavan *et al.*, 2019). With the exception of the analysis in Section 4.4 (see Section 2.4), deviations from climatology (i.e. anomalies) are computed following Fragkoulidis *et al.* (2018). In particular, the mean annual cycle at a given grid point is smoothed by a Fourier decomposition and restriction to the first four harmonics. A separate smooth annual cycle is produced for the four available times of the day (i.e. 0000, 0600, 1200, 1800 UTC) so that the diurnal cycle is taken into account. The anomalies are then computed by subtracting the respective smoothed annual cycle from the 6-hourly full field.

2.1 | EPE definition and classification

The selection of EPEs, which will form the basis for our investigations, follows the methodology that has been described in Part I (Grazzini *et al.*, 2020a). Precipitation measurements in a dense network of 1,762 rain-gauges are first aggregated over the 94 warning areas (WAs) of the Italian Department of Civil Protection (Figure 1). This choice is preferable to regular boxes, since precipitation averages are computed on subregional hydrological basins which are climatologically homogenous. EPEs are then defined as days with daily precipitation greater than or equal to the 99th percentile across one or more WAs, occurring in the period 1979–2015. As in Part I, EPEs are subdivided into three categories based on an unsupervised K-means clustering approach that considers area-averaged values of six thermodynamic and dynamical fields (convective adjustment time-scale *Tau*, convective available potential energy *CAPE*, meridional component of integrated water vapour transport IVTn, θ_{e850}, $\Delta\theta_{e500-850}$, total column water vapour TCWV) described in table 1 of Part I. In contrast to Part I, which is based on ERA-Interim data (Dee *et al.*, 2011), the subdivision of EPEs here is actualized on the new ERA5 dataset. The catalogue of EPE days is very similar to the one of Part I, since the classification is based on area-averaged values and it is not sensitive to small local changes. Next, we compose the lists of independent
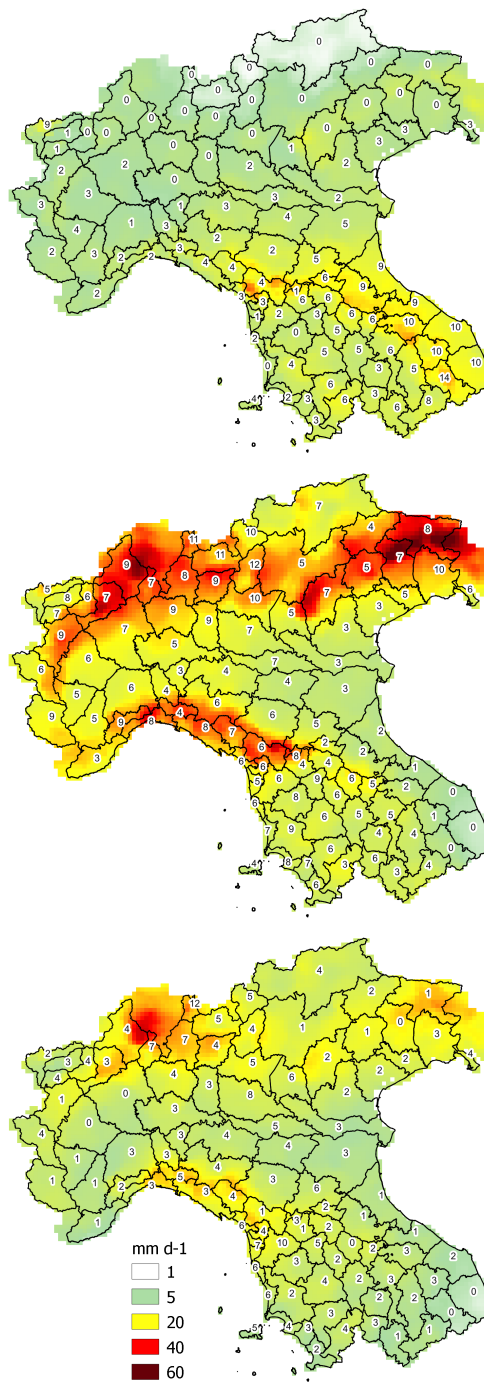

FIGURE 1 Precipitation composites [mm·(24 hr)$^{-1}$] during the 100 representative Cat1 (top), Cat2 (middle), and Cat3 (bottom) EPEs. Warning area boundaries are shown along with the number of exceedances of the 99° of daily precipitation in each warning area

events in each category. For episodes that lasted for more than one consecutive day, we identify the first day of this sequence as the onset of the extreme precipitation event. The next event has to be at least 3 days later. This way, the EPEs we investigate can be considered as distinct events. Given that the resulting lists of independent events in the three EPE categories are not equal in size (287, 248

and 133 events in category 1, 2 and 3, respectively), for the purpose of comparison, a subsample of the 100 most representative cases of each category is selected based on ranking of the Silhouette score (SIL: Rousseeuw, 1987). SIL measures, along each dimension (i.e. each normalized predictor), how tightly the events are grouped inside each cluster (cohesion) compared to the remaining clusters (separation). It ranges from −1 (wrong clustering) to 1 (fully separated and compact clusters) with values equal to 0 indicating that a given element has the same distance from the other cluster centroids (overlapping). Consequently, the 100 cases of each category with the highest SIL score are the cases that are most separated from the other categories and best characterize their cluster.

2.2 | Diagnosis of Rossby wave packet amplitude

The diagnosis of RWP amplitude follows the approach of Zimin *et al.* (2003), with a few distinctions in the input variable and filtering steps. First, the 300 hPa meridional wind anomaly at every latitude is zonally filtered to wavelengths 2,000–10,000 km using a Tukey window in spectral space as in Fragkoulidis *et al.* (2018). Using the anomaly field excludes the effect of stationary waves from the analysis and the zonal filtering restricts to the more relevant scales of a transient RWP evolution, that is, the typically small contribution from transient planetary waves and small-scale features is effectively discarded. Subsequently, a meridional convolution with a Hann window (Harris, 1978) of 7° length at half maximum is applied in order to account for possible unphysical discontinuities from the latitude-wise application of the zonal filtering. Discarding the negative frequencies and applying an inverse Fourier transform to the meridional wind signal at every latitude results in a complex representation of this signal. The modulus of this so-called "analytic signal" corresponds to the envelope, E, of meridional wind, that is, the RWP amplitude. Finally, a weak smoothing is applied to the E field by discarding zonal wavelengths below 4,000 km (see also Fragkoulidis and Wirth, 2020).

2.3 | Statistical significance assessment

Statistical significance in the composite maps and Hovmöller diagrams is assessed using a Monte Carlo approach (e.g. Martius *et al.*, 2008). In particular, the value at a grid point is statistically significant at the α = 0.10 level, if it belongs to the highest or lowest 5% tail of a distribution created by reconstructing the composite 300 times using random selections of an equal number of dates. The assessment of statistical significance in a given field takes the seasonality of EPEs into account by properly restricting the pool the random dates are selected from. In particular, this pool includes the months when more than 10 EPEs of a given category have occurred (Figure 3). For Cat1 EPE composites we draw dates from November, December, January, February, March and April. For Cat2 EPE composites, we draw dates from May, June, September, October and November. Finally, for Cat3 EPE composites, we draw dates from June, July, August and September.

2.4 | PV tendency framework

We investigate the spatio-temporal evolution of the upper-tropospheric flow preceding EPEs by analysing the PV tendencies, as introduced by Teubler and Riemer (2016). This framework was previously applied, among other studies, to investigate the amplification of a North Atlantic ridge–trough couplet, associated with a severe precipitation event on the northern side of the Alps (Piaget *et al.*, 2015).

The framework is based on the hydrostatic form of Ertel's potential vorticity PV on an isentropic surface. Anomalies in PV, PV', are calculated (in contrast to Teubler and Riemer, 2016) as deviations from a background $\overline{PV}$, similar to the one described at the beginning of Section 2. Only for smoothing, a 30-day running mean is used instead of Fourier decomposition. Following the concept of baroclinically coupled Rossby waves (Eady, 1949; Hoskins *et al.*, 1985) the PV anomalies are separated into upper-level and low-level PV anomalies. The associated wind field perturbation is derived by piecewise PV inversion under nonlinear balance (Charney, 1955; Davis, 1992). From that we calculate PV tendencies due to the advection of the PV background by (a) the upper-level wind field perturbation, which physically represents downstream development and by (b) the low-level wind field perturbation, which represents baroclinic interaction. We add the (negligible) advection term by the background flow to (a) and refer to this, in the following, as quasi-barotropic propagation. Additionally we derive the divergent flow by Helmholtz-partitioning. Similar to the advective tendencies from piecewise PV inversion we calculate the advection of the PV background by the divergent flow and additionally the PV tendency accounting for an area change of the anomalies due to divergent flow (compare tendencies from equation 6 in Teubler and Riemer (2020). In the following, a vertical average of the PV tendencies between 315 and 350 K (every 5 K) is considered to account for the seasonal cycle. A more detailed description of the PV tendency
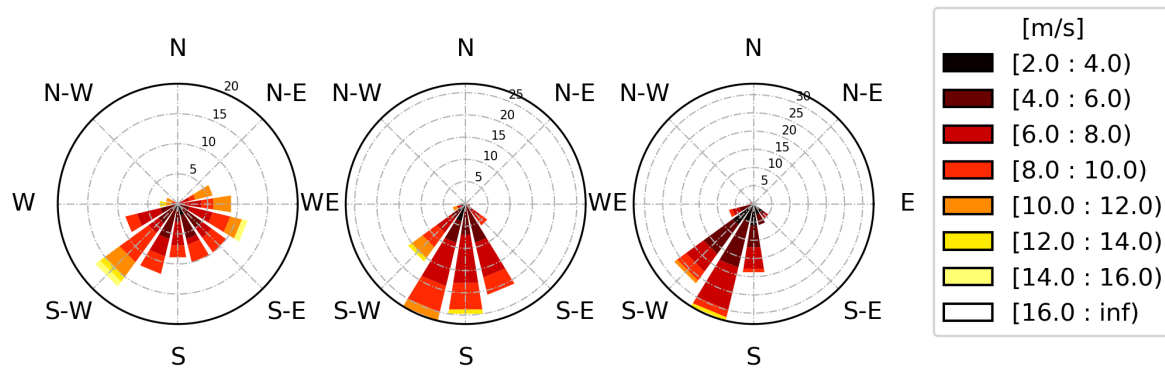
FIGURE 2 Direction and intensity of 850 hPa wind associated with the 100 representative Cat1 (left), Cat2 (middle) and Cat3 (right) EPEs. Spokes indicate the distribution of prevailing wind direction during the EPEs, with their length pointing to the greatest frequency (frequency is shown on the radial contours every 5%). Colour bands are showing mean wind speed in each direction ([m·s^{-1}], see legend). Wind direction and speed are computed as the daily average over the target area which includes the whole of north and central Italy

framework and a comparison to the more commonly used eddy kinetic energy framework can be found in Wirth *et al.* (2018).

3 | EPE CHARACTERISTICS AND UPPER-TROPOSPHERIC WAVINESS

In this section, we discuss the synoptic conditions and monthly distribution associated with the three EPE categories. Furthermore, we examine the linkage between extreme precipitation over northern-central Italy and upper-tropospheric waviness.

3.1 | Precipitation distribution and synoptic analysis

In Figure 1, we show the precipitation composites for the 100 representative cases of each EPE category. The precipitation patterns in the three categories appear consistent with the expected subdivisions and the associated meteorological conditions which are briefly recalled here. Category 1 (Cat1) events originate from frontal structures, with slantwise ascent in warm sectors and warm conveyor belts of Mediterranean cyclones. The associated mechanical orographic uplift of low-level marine, statically stable air typically produces extreme precipitation mostly confined to upwind steep topography. The distinctive feature of Category 2 (Cat2) events is a synergetic combination of frontal uplift and embedded deep convection which produces the most intense and spatially extended EPEs (as shown in Part I by the mean area extension which is double compared to Cat1 events). They are characterized by a stronger southerly flow component and a reduced moist static stability (almost neutral conditions).

Category 3 (Cat3) events are typically not associated with fronts, and precipitation is due to weakly-forced convection (non-equilibrium convective events) in a potentially unstable thermodynamic environment (i.e. with very high CAPE). To facilitate the interpretation of the composites, the number of the 99th percentile threshold exceedances in each warning area is also shown. Since an EPE is defined as a day in which one or more WAs exceed the 99th percentile threshold of daily rain accumulation, those numbers indicate which areas contributed most in the EPEs selection. As can be seen for example in the Cat1 case, most of the EPEs are associated with extreme rainfall amounts in central Italy and specifically in the Adriatic WAs, presumably due to the easterly low-level winds. Regarding Cat2 events, the situation is different with a higher frequency of extreme rainfall found in Tuscany and south-facing regions on the Apennines and the Alps. The precipitation composite (Figure 1, middle panel), shows higher intensities over the southern part of the Alpine region and the Apennines. Cat2 events are known to produce the stronger impact in terms of floods and damages (see Part I and Grazzini *et al.* (2020b)). For Cat3, the exceedance frequency is rather homogeneous with relative maxima over the central Alps and northern Apennines. The mean direction and intensity of the 850 hPa wind are shown in Figure 2 in the form of wind roses. The low-level wind associated with Cat1 (left panel) shows an almost even distribution of prevailing direction spanning the two southern quadrants, from easterly to westerly direction, with frequency and intensity maxima in the southwest direction. However, easterly winds seem to be as frequent as westerly winds, which can explain the high frequency exceedance of the precipitation threshold in the Adriatic regions. As shown in Figure 3d, Cat1 events typically occur during the colder months (November to April). Precipitation and wind distribution in this category are in fact

in agreement with typical winter surface cyclone development in the area with minima moving east, from the Tyrrhenian sea toward the Adriatic sea, preceded by southwesterly winds and followed by easterly winds.

In contrast, Cat2 events occur mostly in May, June and autumn, and a predominant southerly direction is clearly visible in the middle panel of Figure 2. Cat3 events are concentrated in the period from June to September with a prevailing southwesterly direction. Cat2 and Cat3 events are characterized by a neutrally stable or unstable environment (see Part I, figure 8), respectively, so the flow is less confined at low levels.

Composites of Z at 500 hPa (Figure 3(a–c)), show that a trough over western Europe is present in all three categories. However, the trough in Cat2 events is sharper and more to the west (centred at the prime meridian) than Cat1. The associated surface cyclone over the central Mediterranean in Cat2 is weaker than Cat1, but shifted more to the east relative to the trough axis, pointing therefore to a stronger baroclinicity. A pronounced anomaly of integrated water vapour transport toward the target domain (northern-central Italy) is evident in all three categories, but more pronounced in Cat2. The IVT magnitude is mostly associated with its meridional component, IVTn, which is much higher than normal, especially in Cat2 where it exceeds the mean values for non-EPE days by more than two standard deviations (not shown). The presence of such IVT anomalies at the synoptic scale points to the pivotal role of upper-level wave amplitude in achieving the strong meridional moisture transport observed. High moisture convergence is a necessary requirement to achieve intense and widespread precipitation (as in Cat2) since the area extension is critically dependent on large-scale convergence of moisture (Loriaux et al., 2017).

3.2 | Linkage between EPE occurrence and RWPs

In this section we aim to quantify the linkage between EPEs in northern-central Italy and RWPs by first assessing the association of heavy precipitation probability with waviness in the upper-tropospheric flow. In this regard, we use two upper-tropospheric waviness indicators: (a) the envelope, E, of meridional wind at 300 hPa, and (b) the absolute value of PV anomaly, |PV′|, at 330 K. The first one constitutes a phase-independent measure of the meridional wind amplitude, while the second is a measure of waviness in the upper-troposphere as reflected in the deviations of the PV field from climatology.

In order to introduce the concept of the aforementioned indicators and the statistical analysis that follows,

in Figure 4 we show the dynamical evolution leading to the Piedmont flood of November 1994, a typical example of Cat2 events, described in detail in Grazzini et al. (2020b). Depicted are the meridional wind at 300 hPa, the corresponding E, and the 2PVU (PV units) contour at 330 K on the days leading to the event. The evolution of E highlights the regions where the RWP amplitude is large, which is also reflected in the large meridional wind anomaly (v') values and the associated succession of troughs and ridges that result in a wavy 4PVU contour. Days D-4 and D-3 are characterized by isolated and incoherent disturbances over the North Pacific and a weaker disturbance over North America that slowly propagates eastward and appears to strengthen. On D-2, an apparent rapid intensification of the latter results in the formation of a large-amplitude wave packet over the North Atlantic, the leading edge of which is already approaching the British Isles. Meanwhile, the North Pacific disturbances appear to form a more coherent wave packet that reaches North America but does not directly affect the centre of action of the North Atlantic. On D-1, the North Atlantic wave packet has progressed further downstream and is characterized by a strong trough that dominates the flow over western Europe. From D-1 to D0 (onset of the EPE), this trough elongates further, appears to remain quasi-stationary, and obtains a north–south orientation while the leading edge of the wave packet approaches Siberia. As will be discussed later, such a PV streamer structure modulates effectively the regional flow and moisture transport and can thus play an important role in determining the onset and intensity of the EPE. Finally, an apparent wave breaking between D0 and D+1 over western Europe is clearly depicted in the 4PVU contour and marks the decay of the wave packet.

The statistical analysis that follows takes into account that the envelope, E, of meridional wind at 300 hPa is well-suited for RWPs in their almost-plane stage (Fragkoulidis and Wirth, 2020), whereas PV anomaly constitutes a better indicator of upper-level forcing in the later stages of wave overturning and breaking (see also Ghinassi et al., 2018). Therefore, in order to assess the relation between upper-tropospheric waviness and EPE occurrence, we perform two separate regression analyses that involve E on D-2 and |PV′| on D0 averaged over two different areas as shown in Figure 5. The absolute value of PV anomalies is used in order to avoid cancellations between positive and negative anomalies in the area-averaging. The two analyses will involve the daily aggregated precipitation in northern-central Italy as well as the EPE occurrence of a specific category.

For each day in the 1979–2015 period, the daily-mean E is averaged over the 38°–62°N, 22°W–2°E area (dashed rectangle in Figure 5) and the resulting sample is split into 10 equally-sized bins based on the nine deciles of
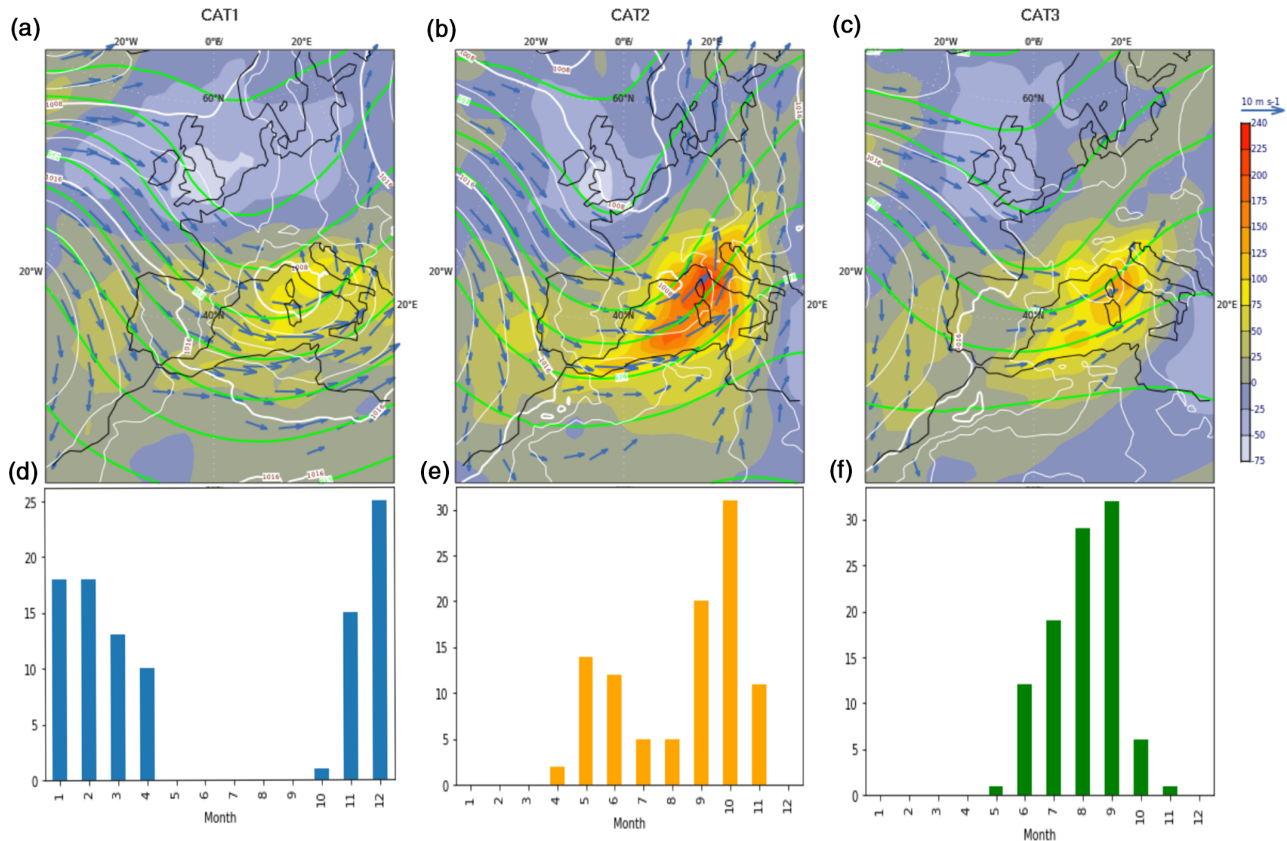
FIGURE 3 Composite maps during the 100 representative (a) Cat1, (b) Cat2 and (c) Cat3 EPEs of geopotential height at 500 hPa (green solid contours, every 6 gpdam), mean-sea-level pressure (white solid contours, every 2 hPa), integrated water vapour transport (IVT) anomaly (colour fill, kg m^{-1} s^{-1}), and wind speed at 850 hPa (blue arrows, m s^{-1}). (d–f) Monthly distributions of the three EPE categories (number of occurrencies)

area-averaged E. The first bin contains the days when E is between the minimum and the 10th percentile, the second bin contains the days with E between the 10th and the 20th percentile, etc. Subsequently, the total precipitation, with a lag of +2 days, is averaged over the 94 available warning areas in northern-central Italy. Figure 6a shows in black dots the percentage of days in each E-bin that surpass the 90th percentile of average precipitation over northern-central Italy, or else, the probability for heavy precipitation over the domain. Note that this is different from EPEs which are defined as days with local extremes on warning areas. The heavy precipitation frequency increases with increasing E and approximately 40% of heavy precipitation events occur at the upper two E-bins. In the same way, the probability for heavy precipitation is evaluated against the contemporary |PV′| at 330 K averaged over the 38°–50°N, 4°–16°E area (solid rectangle in Figure 5) and displayed in Figure 6b. A clear connection is also found in this case with approximately 36% of heavy precipitation events occurring at the upper two |PV′|-bins. Repeating the analysis in this area for E instead of |PV′| results in a worse connection, with only

about 25% of heavy precipitation events at the upper two E-bins (not shown). The fact that the connection between E and northern-central Italy heavy precipitation is better for the dashed rectangle on Day −2 than the solid rectangle in Day 0, suggests that heavy precipitation events in northern-central Italy are typically associated with an upstream RWP that amplifies over the North Atlantic and subsequently breaks over western Europe, as illustrated in the Piedmont flood case.

Next, it is worth investigating whether this relation holds for all three types of EPEs. The blue, orange and green dots in Figure 6 correspond to the percentage of days in each E-bin that is associated with a Cat 1, 2 and 3 EPE, respectively. The probability for Cat 1 and 2 EPEs increases with a rate that is only slightly higher for Cat 1 in the case of E and similar in the case of |PV′|. Although there is some waviness in the flow during Cat 3 EPEs (Figure 3c), their occurrence is not increasing with E. The poor correlation in this category is consistent with the fact that Cat 3 events are mostly associated with high thermodynamic instability and non-equilibrium convection (or weakly forced convection), in which the interaction between the synoptic
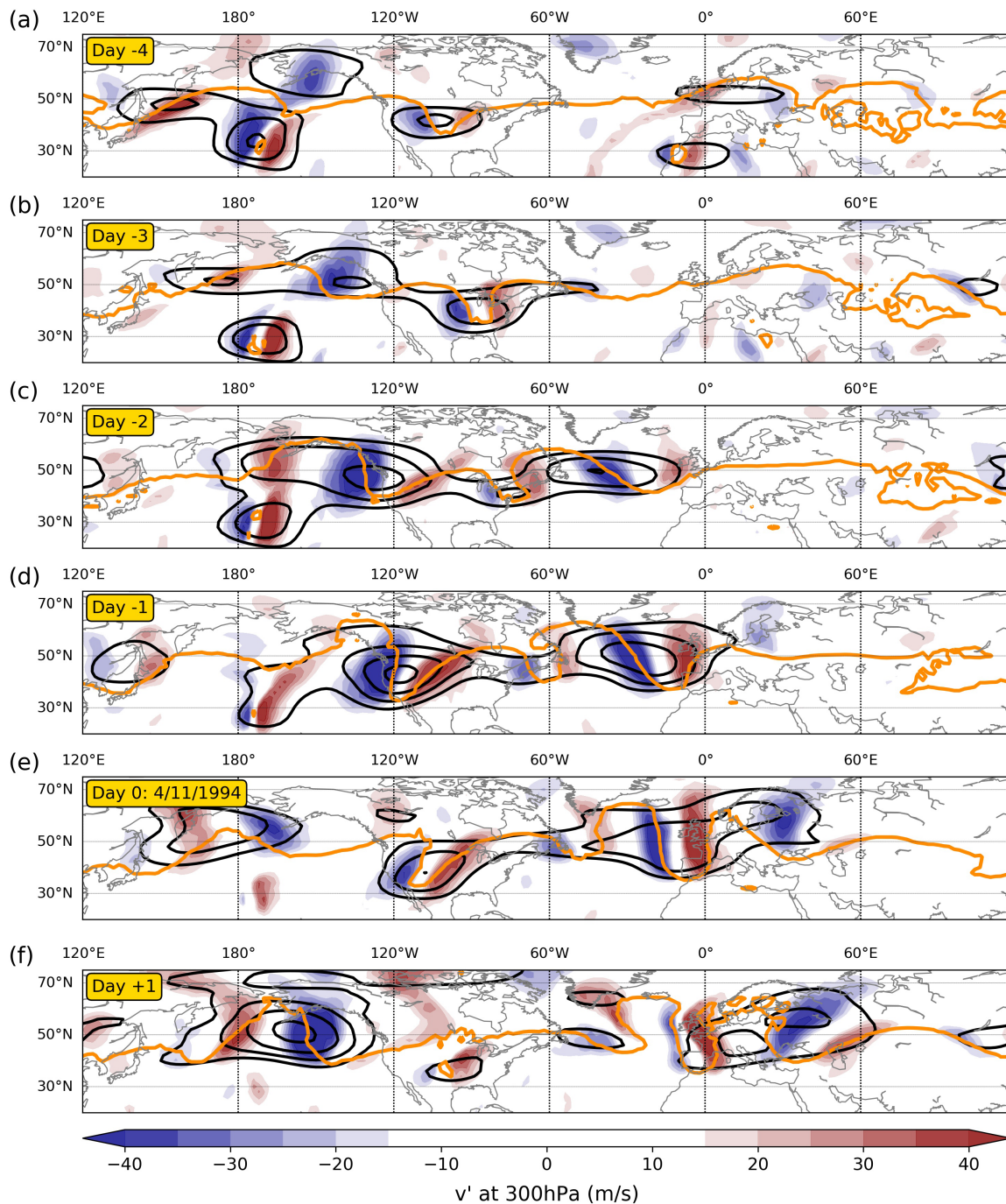
FIGURE 4 Evolution of the upper-tropospheric flow leading to the November 1994 Piedmont flood. The panels depict mean daily values of meridional wind at 300 hPa (colour fill, m·s⁻¹), E at 300 hPa (black contours every 10 m·s⁻¹ starting from 25 m·s⁻¹), and the 4PVU isoline at 330 K (orange contour) at (a) 31 October 1994 (day −4), (b) 1 November 1994 (day −3), (c) 2 November 1994 (day −2), (d) 3 November 1994 (day −1), (e) 4 November 1994 (day 0), and (f) 5 November 1994 (day +1)

flow and convection is weaker (Done *et al.*, 2006; Zimmer *et al.*, 2011). The weak relation also suggests that these events are less predictable, since severe convection can be triggered, in a very unstable environment, even with small amplitude waves or due to local thermal circulations. It should be noted that, generally, the probabilities of Cat 1, 2 and 3 EPE occurrence in each E-bin do not sum up to

the heavy precipitation probability (black dots), since the former are defined with stricter criteria (days with at least one warning area with daily precipitation above the 99th percentile). Finally, we notice that the probability of EPEs grows slightly more rapidly with E for mountainous as opposed to low elevation warning areas (not shown). This
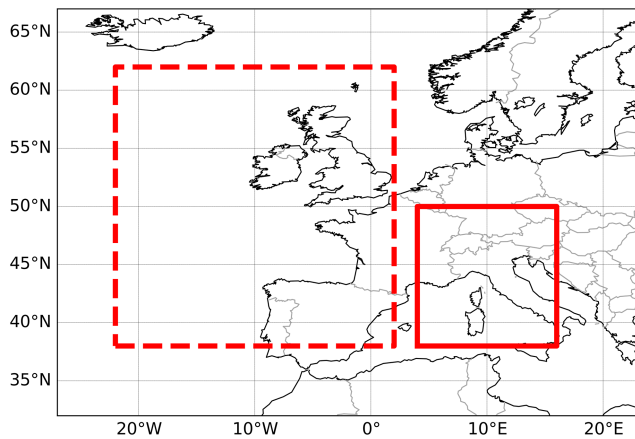
FIGURE 5 Areas used for averaging E at D-2 (dashed rectangle; 38°–62°N, 22°W–2°E) and |PV′| at D0 (solid rectangle; 38°–50°N, 4°–16°E)

implies that, due to the stronger interaction with orography, the mountainous regions are more sensitive to RWP amplitude.

The above results do not change substantially for slight variations in the size and location of the two areas in Figure 5. Using a single vertical level, as is done here for simplicity, may constitute a limitation in cases when the wave packet evolution is characterized by pronounced variability in the vertical direction. However, the results of the regression analyses in Figure 6 remain quantitatively similar when using the maximum E between the 200, 300 and 400 hPa levels and the maximum |PV′| between the 315 and 350 K levels (with 5 K increment) at every grid point. Finally, it has to be noted that although many times these waviness metrics attain large values over Europe, heavy precipitation or EPEs in northern-central Italy are not observed simply because the phasing of the trough–ridge sequence is not the right one (Figure 3). Therefore, higher probabilities are to be expected when we restrict to cases with a trough over western Europe.

4 | DYNAMICAL EVOLUTION

4.1 | RWP composites

In the previous section, we have shown that there is a statistical relation between large-scale upper-tropospheric waves and the probability of EPEs. In this section, we investigate in more detail the dynamics, and in particular the RWP characteristics leading to the three different categories of EPEs. We want to test the hypothesis that the three different categories exhibit specific propagation patterns of the precursor RWPs. In this respect, Hovmöller diagrams of the upper-tropospheric meridional

wind are well-suited to depict the main properties of the spatio-temporal RWP evolution (Martius *et al.*, 2006b; Persson, 2017). Unlike the amplitude measure used in the previous section, they provide an indication for the preferred phase during the RWP evolution, which is critical for the occurrence of EPEs. To this end, composite Hovmöller diagrams of v' at 300 hPa are constructed for the 100 representative cases of each EPE category (see Section 2.1) and the emerging patterns are shown in Figure 7. Evidently, a large-scale wave feature is recognizable in all categories at Day 0, but the characteristics of the spatio-temporal evolution of the RWPs are different. In the following, T_0 (Trough at Day 0) will refer to the trough over western Europe, directly associated with EPEs (Figure 3), and T_U (Trough Upstream) will refer to the upstream trough forming off the eastern coast of North America.

In Cat1 events, there is a statistically significant far-upstream RWP signal that is first detected over the eastern Pacific 5–6 days before the event and propagates toward Europe at a zonal group velocity of approximately $30° \cdot day^{-1}$ (Figure 7; group velocity can be roughly estimated as the slope of a hypothetical line that connects the areas of positive and negative v' in the Hovmöller diagram). On days −1 to +1 of the events, the composite RWP spans approximately 150° in longitude with strong northerlies over the eastern North Atlantic and southerlies over Europe signifying the pronounced trough seen in Figure 3. A few days prior to the emergence of this RWP, a secondary RWP of weaker magnitude and lower group velocity but with the same phase as the primary RWP is also evident in the composite Hovmöller diagram. The two wave packets merge over the target region forming the trough T_0. This suggests that the amplification and quasi-stationarity of T_0 may sometimes be associated with a sequence of RWPs of the same phasing, that induces a recurrent amplification of troughs and ridges at the same longitudes. The mechanism of RWPs recurrence, as a factor explaining the stationarity and amplification of a particular element of a wave pattern, has been shown by Barton *et al.* (2016) and Röthlisberger *et al.* (2019). Individual troughs and ridges are characterized by high phase speed ($7° \cdot day^{-1}$), extending almost uniformly from the North Pacific to Europe. However, the situation over Europe is characterized by a substantially reduced phase speed (waves slow down, becoming almost stationary) in conjunction with wave amplification and possible wave breaking. Although this sequence of events arises from the analysis of the composite Hovmöller diagram, it appears consistent with the evolution of individual cases.

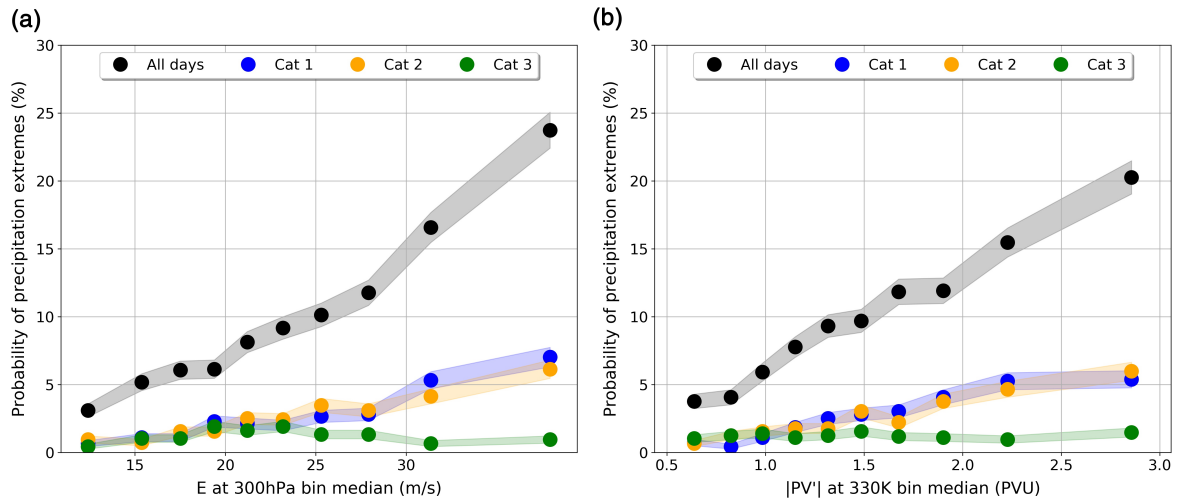The composite RWP signal in Cat2 events is more confined in longitude (Figure 7b) compared to Cat1, and

(a)

(b)

FIGURE 6 (a) Probability of heavy precipitation events in northern-central Italy as a function of the area-averaged E (m·s⁻¹) (dashed rectangle in Figure 5) at a lag of 2 days. The black dots correspond to the percentage of days next within each E-bin of size N that exceeds the 90th percentile in the average precipitation over the 94 warning areas. The dots in the x-axis are placed at the median of E in each bin. Assuming that next corresponds to the sample mean of a Poisson distribution, and that many measurements have been done resulting in a Poisson distribution of sample means, the associated uncertainty (shaded range) is based on the standard error of this distribution: the blue, orange and green dots correspond to the percentage of days within each E-bin that are characterized as a category 1, 2 and 3 EPE respectively. (b) Same as (a) but now the probability of heavy precipitation events is evaluated against the contemporary area-averaged $|PV'|$ at 330 K (solid rectangle in Figure 5)
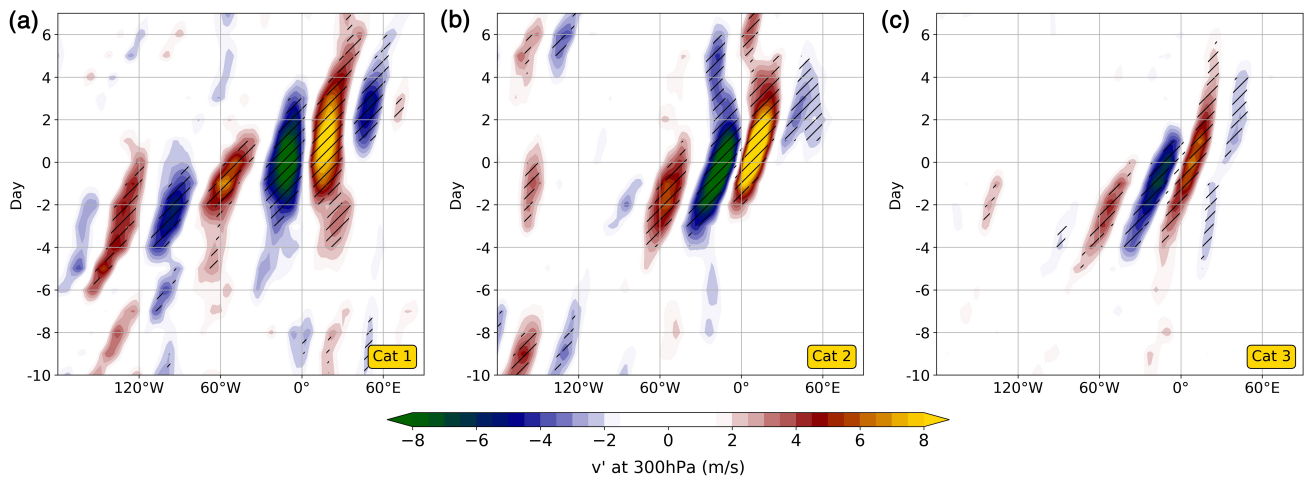
(a)

(b)

(c)

FIGURE 7 Composite Hovmöller plots of v' at 300 hPa (colour fill, m·s⁻¹; positive meridional wind corresponds to northward direction) during the 100 representative cases of (a) Cat1, (b) Cat2 and (c) Cat3 EPEs. For every longitude, v' is meridionally averaged over the 30°–60° latitude band. The hatches indicate statistical significance at the 0.10 level (see Section 2.3)

extends from the North American east coast to Europe. This implies that in Cat2 events there is either no in-phase wave propagation west of 90°W (so the signal in the composite is reduced through destructive interference), or there is rapid amplification over the North Atlantic without a significant far-upstream precursor. The amplification starts in T_u just west of 60°W, followed by the development of T_0 around the Greenwich meridian, in the correct phase

to produce strong water vapour convergence and precipitation to the south of the Alps. Therefore, the processes driving the amplification of the North Atlantic ridge may play a key role in determining the evolution and specific positioning of the downstream trough T_0.

The magnitude of the meridional wind anomaly associated with T_0 and T_U is larger in Cat2 events than the other two categories. Notably, the meridional wind anomaly couplet over Europe is not stationary as in Cat1 events but
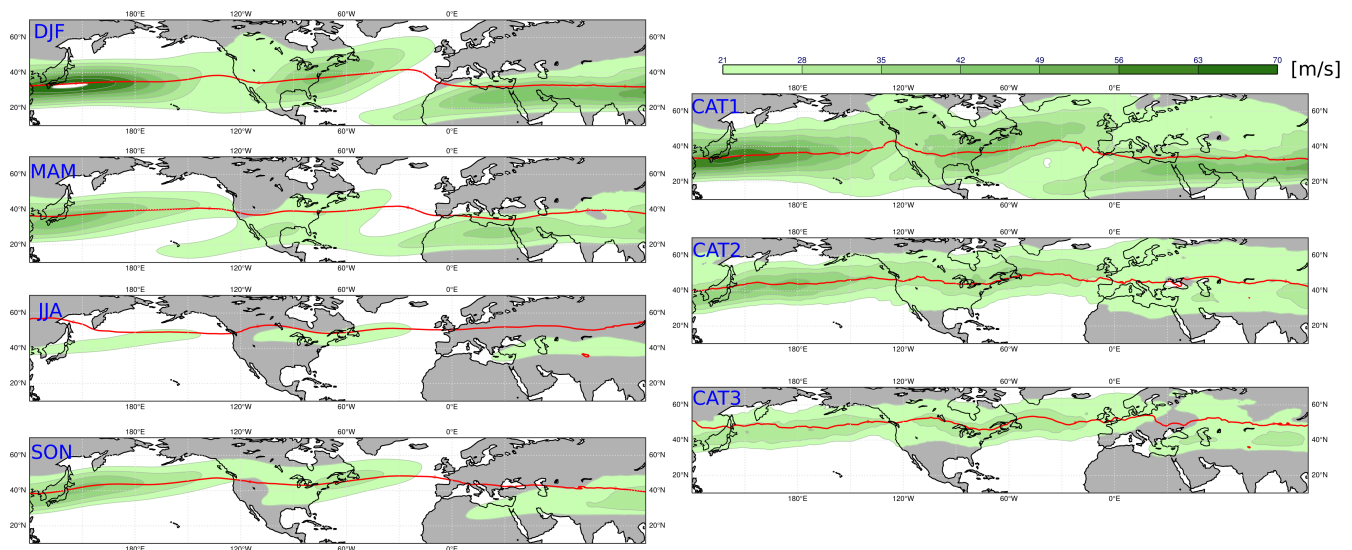
FIGURE 8 Composites of wind speed (m·s^{-1}) at 250 hPa (colour fill) and 2PVU contour at 325 K isosurface (red contour). Panels on the left depict the seasonal composites (all days of the season labelled on the top left of each map), while the panels on the right show composites centred 4 days prior to (i.e. on D-4) the 100 representative EPEs of each category

has a phase speed of 5–7°·day^{-1}. Furthermore, the proximity between the northerly and southerly bands in Cat2 events implies that the typical wavelength of T_0 is smaller than in Cat1 events. Group velocity is generally lower than in Cat1 while the phase speed is not uniform in time and longitude.

Despite the visual impression of the composite, individual Cat2 events do show a connection between the North Pacific and North Atlantic storm tracks, as visible in the example case of the Piedmont flood. We suggest therefore that prior to some Cat2 EPEs, waviness over the Pacific may be out of phase but still enhanced and capable of seeding the North Atlantic storm track. Once the composite RWP signal in Cat2 has reached the North Atlantic a strong coherent amplification is noticeable.

Although largely associated with *in situ* non-equilibrium convection (Grazzini *et al.*, 2020a), Cat3 events show a similar composite RWP signal over the North Atlantic and Europe as in Cat2 (Figure 7c), but with lower amplitude. Relative to the other two categories, the RWP for Cat3 is characterized by a higher phase speed and smaller zonal wavelength.

4.2 | Category composites versus seasonal composites

After a first account on the RWP properties associated with the three EPE categories, it is worth investigating the role of the background flow seasonality in this respect. The natural tendency of the upper troposphere to form

waveguides for the propagation of RWPs has been investigated before. The emergence and efficiency of these waveguides essentially depend on the strength and shape of the jet stream (e.g. Manola *et al.*, 2013; Wirth *et al.*, 2018; Wirth, 2020). Idealized studies of Rossby wave propagation (Hoskins and Ambrizzi, 1993; Branstator, 2002) show that weak jets (associated with weak PV gradients) are typically associated with RWP propagation along great circles, whereas strong zonal jets lead to zonal ducting and longer propagation of the RWPs. The seasonal variability of the jet is associated with a corresponding variability in the mean RWP properties (Fragkoulidis and Wirth, 2020).

Previous studies have shown that the properties of the RWP precursor signal of EPEs in the Alpine area have a seasonal variability (Grazzini, 2007; Martius *et al.*, 2008). In the Martius *et al.* (2008) study in particular, composites of autumn and winter reveal a long and coherent RWP signal that is detectable over the North Pacific up to 7 days prior to the precipitation event. During spring, however, these studies report a short-lived equatorward propagation initiated in the western North Atlantic about 4 days prior to the event. It is therefore interesting to investigate whether the characteristic RWP properties of each EPE category are purely dependent on the period of the year they occur in. To this end, we first compare the jet composites of the three EPE categories with the respective seasonal climatologies, which reflect the annual cycle of the climatological waveguides.

We compare seasonal jet speed composites (all days) to jet speed composites 4 days prior to the occurrence of EPEs (Figure 8). The lag of 4 days allows us to focus on the jet properties prior to the direct influence by the
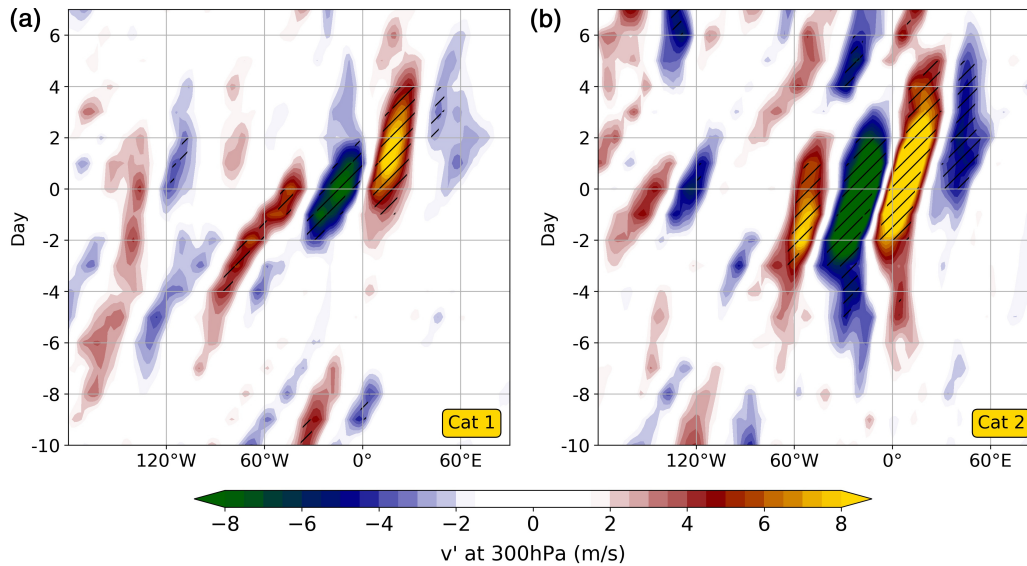
FIGURE 9 Composite Hovmöller plots of v' at 300 hPa, as in Figure 7, but for the (a) 59 Cat1 and (b) 35 Cat2 EPEs that occurred in November

wave associated with the EPE. Nevertheless, the following results do not change substantially for slightly different lags. The composite prior to Cat1 cases, which mostly occur in winter and late autumn (Figure 3d), is similar to the December–February (DJF) composite. An exception is that the Cat1 jet extends more towards Europe and is more intense and continuous over the continental USA, a characteristic which is common to the composites of all EPE categories. The fact that the Cat1 jet composite is similar to the DJF seasonal composite, and that the RWP Cat1 composite (Figure 7a) is similar to the Martius *et al.* (2008) winter composite, suggests that EPEs of this category are not too distinct from the typical winter circulation properties. In contrast, the Cat2 jet composite (Figure 8, middle right panel), instead, differs from the March–May (MAM) and September–November (SON) climatologies, while the Cat3 jet composite is similar to Cat2 but slightly weaker. Finally, we also note the prominent presence of the subtropical jet over the Mediterranean and North Africa in Cat1 events, while this is not the case in either the Cat2 or Cat3 composites.

The above might imply that in the transition seasons the large-scale flow associated with EPEs can vary substantially from the mean, sustaining different types of propagation according to the strength of the meridional PV gradient. To further investigate this point, we produce RWP composites based on all EPE cases (not just the 100 representative ones) that occurred in November, a month when both Cat1 and Cat2 EPEs are frequent. In particular, out of the 95 November EPEs, 59 are Cat1, 35 are Cat2, and 1 is Cat3. Therefore we can test whether in the same month there can be differences in the RWP propagation

associated with the two EPE categories. Indeed, Figure 9 shows distinct propagation patterns for November Cat1 and Cat2 EPEs, with a marked difference in the Pacific precursor part and the amplification over the North Atlantic. As in the full composite (Figure 7), Cat2 composite RWPs are still more confined in longitude. As a side note, June and September are also months when EPEs are not characterized by a distinctly preferable category (Figure 3).

4.3 | Water vapour transport and wave amplification over the Atlantic sector

In this section, we investigate the factors behind the strong amplification observed over the North Atlantic, that is evident in all categories and especially pronounced during Cat2 events, as seen in Figure 7. A strong amplification of the North Atlantic ridge is in fact a necessary condition for the evolution of the trough over western Europe into an elongated structure, able to drive significant water vapour transport toward Europe (Piaget *et al.*, 2015; Scoccimarro *et al.*, 2018). Although ridges are typically wider in longitude than troughs, as expected from the nonlinear dry primitive equations (Hoskins, 1975; Snyder *et al.*, 1991), Teubler and Riemer (2020) have shown that divergent outflow tends to increase ridge amplitude and to decrease trough amplitude systematically. Here we aim to address factors that further influence this asymmetry and that may vary between the EPE categories.

Many studies have shown the effect of diabatic heating in modifying the intensity of PV streamers and Rossby wave evolution downstream (Wernli and Davies, 1997;
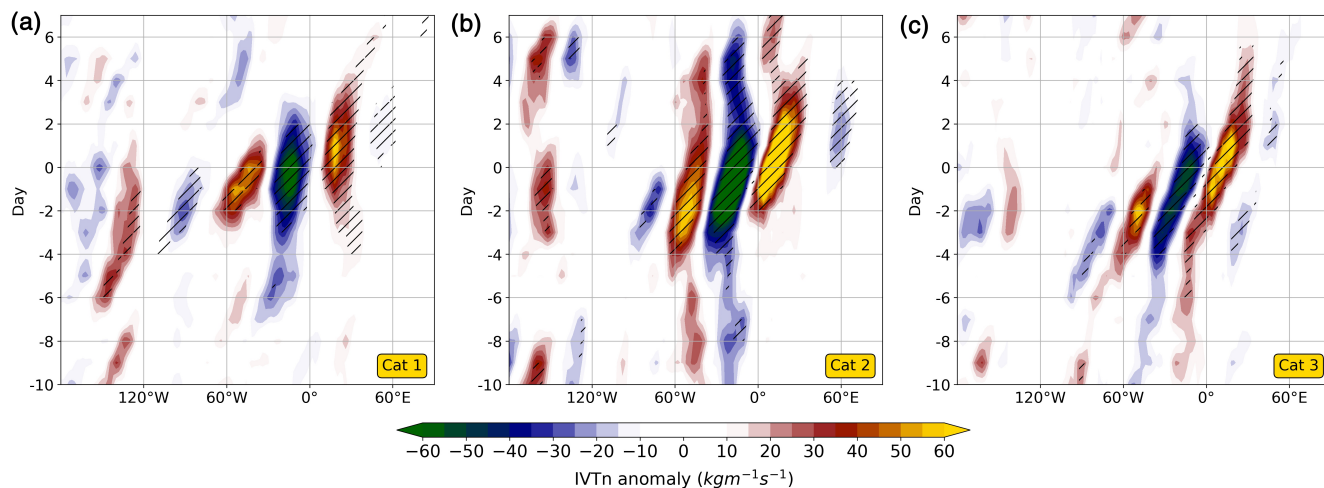
FIGURE 10 Composite Hovmöller plots of IVTn anomaly (colour fill, kg·m⁻¹·s⁻¹) during the 100 representative cases of (a) Cat1, (b) Cat2 and (c) Cat3 EPEs. For every longitude, IVTn anomaly is meridionally averaged over the 30°–60° latitude band. The hatches indicate statistical significance at the 0.10 level

Grams and Archambault, 2016; Grams *et al.*, 2018). This occurs via the injection of low-PV air into the upper troposphere in a deep ascent of moist air streams which can originate from WCBs within extratropical cyclones and their embedded convection, or extratropical transition of tropical cyclones. The resulting upper-level negative PV anomaly can intensify the ridge downstream of the trough, strengthen the PV gradient and in general amplify the meridional elongation of the pre-existing streamer downstream of the ridge (Martius *et al.*, 2008). Numerical experiments with reduced meridional moisture transport and latent heat release lead to waves of substantially weaker amplitude (e.g. Grams and Archambault, 2016). Strong IVT convergence is, therefore, a typical precondition to achieve strong ridge amplification downstream on the target region; a feature that is characteristic of Cat2 events as will be shown later. Following this hypothesis, in this section we investigate the environment of the T_U system in the different categories, in search of mechanisms explaining the differences in the North Atlantic ridge amplification and the associated downstream development. In the next Section (4.4) we evaluate the contribution of different physical processes by adopting the PV tendency framework introduced in Section 2.4.

In Figure 10, we display composite Hovmöller diagrams of the meridional IVT (IVTn) anomaly. The first striking difference between the categories is the strong meridional water vapour fluxes occurring on the North Atlantic basin in Cat 2, beginning about 4 days before EPEs. Cat 1 EPEs are instead characterized by transient meridional IVT associated with a coherent and long-lasting wave packet that appears to form in the Pacific (180°W) at D-6. Cat 3 EPEs are similar to Cat 2, but with

weaker – although still statistically significant – water vapour transport.

In order to complement the information of Figure 10, in Figure 11 we display the North Atlantic 500 hPa geopotential height (full field and anomaly) and IVT anomaly composites at D-4, D-2 and D0. As a reference, the position of T_u is marked on Figure 11, whenever a close negative anomaly isoline (dashed) is evident. At D-4 in the Cat1 composite (Figure 11g) we note a stronger meridional height gradient compared to Cat2 and Cat3 (Figure 11h,i), which is consistent with the higher jet speed observed in Figure 8. An upstream trough (T_u) is located over Hudson Bay, and there is no apparent IVT anomaly or ridging over the North Atlantic associated with it. It is only at D-2 (Figure 11d), when it reaches the North Atlantic, that T_u starts to intensify, in association with a moderate positive IVT anomaly on its ascending branch and the strengthening of the wave downstream, as reflected in the geopotential height anomaly contours. The wave amplification continues until D0 when a particularly strong trough (T_0) dominates the flow over Europe (Figure 11a).

At D-4 for Cat2 EPEs, the T_u over North America is too weak to produce a closed contour in Figure 11h (weaker than −2gpdam), but positive IVT and geopotential height anomalies are apparent over the North Atlantic. A stronger amplification of the associated North Atlantic ridge is apparent on D-2 of Cat2 (Figure 11e) compared to Cat1, as indicated by the stronger positive geopotential anomaly. Furthermore, the Cat2 composite height anomalies over the North Atlantic imply waves of smaller wavelength than those of Cat1 events (as also suggested by the Hovmöller diagrams in Figure 7) and appear to be
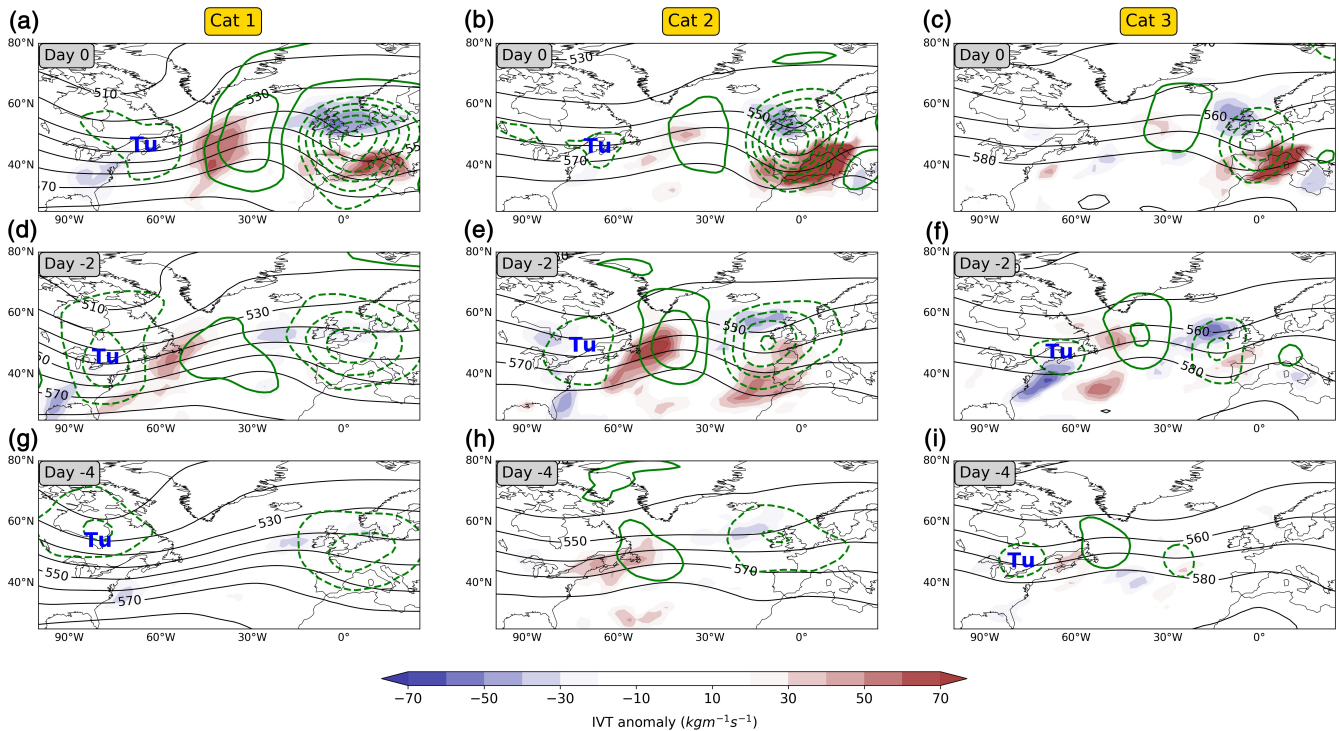
FIGURE 11 Composite maps of the IVT magnitude anomaly (colour fill, kg·m⁻¹·s⁻¹), geopotential height at 500 hPa (black contours every 10 gpdam), and geopotential height anomaly at 500 hPa (green contours at ±[2, 4, 6, …] gpdam; solid: positive anomalies, dashed: negative anomalies) at day 0 of the 100 representative (a) Cat1, (b) Cat2 and (c) Cat3 EPEs. Panels (d–f) correspond to day −2 and panels (g–i) correspond to day −4 of the three EPE categories respectively. The approximate position of the Tu trough is marked in blue

less influenced by upstream waves coming from North America. The latter hints at a more local forcing over the northern edge of the western boundary ocean current, as opposed to the Cat1 flow evolution described before. Finally, the large-scale flow prior to Cat3 EPEs is characterized by an overall weaker wave packet that amplifies slowly and has a shorter wavelength than the other two categories (see also Figure 7). In the next section, we investigate which processes are responsible for the more vigorous North Atlantic ridge amplification prior to Cat2 EPEs.

4.4 | PV tendency analysis of the precursor wave

In this section we investigate, in a composite sense, the contribution of individual processes, including latent heat release, to the spatio-temporal evolution of T_u and the respective downstream ridge. Since latent heating is not directly available in the ERA5 reanalysis, we employ a proxy based on the Lagrangian change in column water vapour: LHRproxy = $-L*(\partial IWV/\partial t + \nabla \cdot IVT)$ (see equation [3] from Trenberth and Solomon (1994)). L denotes the latent heat of vaporization of water, IWV the

vertically integrated water vapour content, and IVT the vertically integrated water vapour transport as described before.

We will consider PV tendencies showing the contribution of quasi-barotropic propagation, baroclinic interaction, and divergent outflow to PV amplitude and neglect contributions to deformation and wave breaking. The role of these processes can be understood conceptually in terms of downstream baroclinic development in the PV framework (e.g. Wirth *et al.*, 2018). Downstream of an existing trough, a new ridge is created at the leading edge of an RWP due to quasi-barotropic (negative) PV advection. Subsequently, baroclinic interaction with the low-level temperature gradient is established, which reinforces the upper-level ridge by PV advection associated with low-level temperature anomalies. Baroclinic interaction is also associated with rising motions which will produce upper-tropospheric divergent outflow. Teubler and Riemer (2020) argued that such a ridge evolution is more precisely described as a downstream *moist*-baroclinic development, so as to include the contribution from moist processes. They showed that the impact of latent heat release on the PV amplitude is most effectively communicated by the enhancement of vertical motion and hence the divergent outflow.

FIGURE 12 (a–e) Composite maps of PV anomalies (blue-grey shading) and tendencies of the 100 representative Cat1 EPEs on days 0, −1, −2, −3 and −4. LHRproxy is shown by green coloured dots (only positive values shown). PV tendencies due to quasi-barotropic propagation (blue contours at ±[0.5, 1, 1.5, 2] PVU·day^{-1}), baroclinic interaction (orange contours at ±[0.04, 0.06, 0.08, 0.12] PVU·day^{-1}), and divergent outflow (red-purple shading). Solid contours refer to positive tendencies and dashed contours refer to negative tendencies. Grey lines refer to temperature at 850 hPa (every 10 K). The PV field and its tendencies correspond to the mean values between the 315–350 K isentropic levels
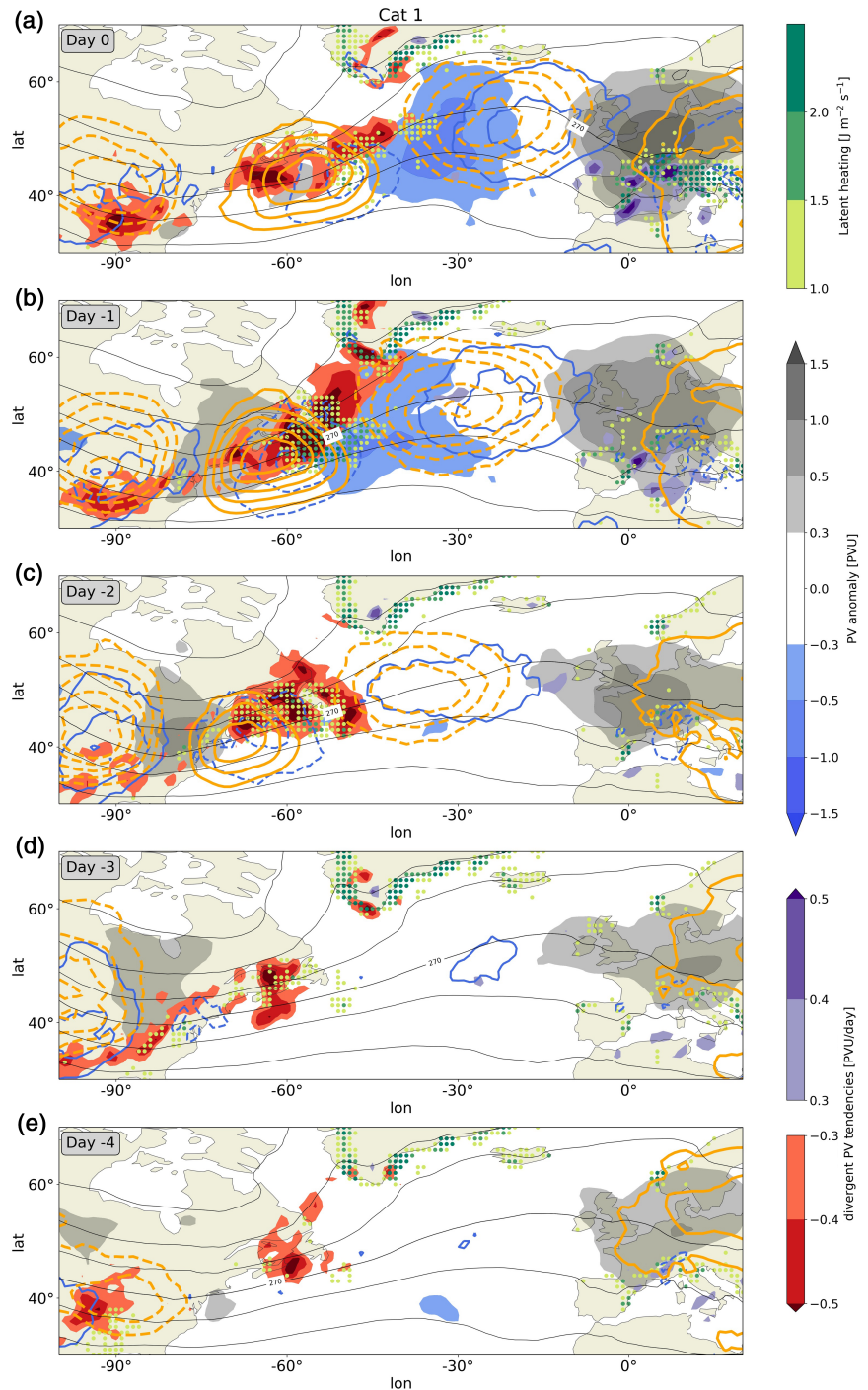
In Figures 12–14 we show composite maps of PV anomaly, LHRproxy, and PV tendencies at time lags from D0 to D-4 prior to Cat1, Cat2 and Cat3 EPEs. Starting with Cat1 events at D-4 (Figure 12e), the incoming baroclinic RWP (Figure 7a) can be identified over North America by the positive quasi-barotropic PV tendencies (solid blue contours) and negative baroclinic PV tendencies (dashed orange contour). However, the collocation of these tendencies is not favourable for mutual growth by baroclinic interaction. We also note the positive

PV anomaly (grey shading) and baroclinic PV tendencies over Europe, as a remnant of a previous wave over Europe (also evident in Figures 7a and 11g). The initially weak divergent outflow tendencies (red shading) and latent heating (LHRproxy indicated by coloured dots) at the North American east coast increase from D-4 to D-3 but do not have an apparent contribution to the North Atlantic ridge evolution. At D-2, however, the ridge development around 45°W is subject to moist-baroclinic development as indicated by the combination of enhanced
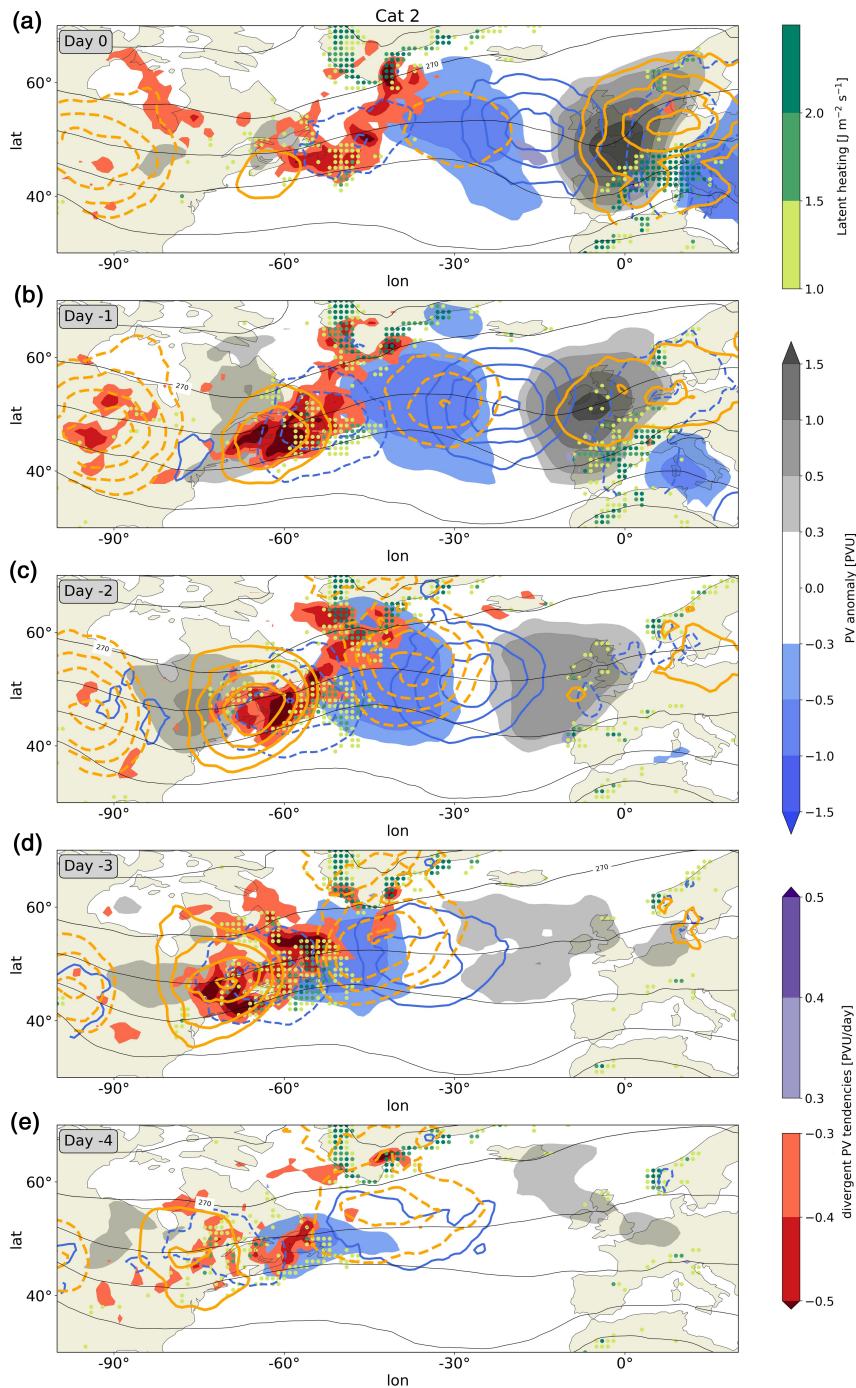
FIGURE 13 (a–e) The same as Figure 12 but for the composite of the 100 representative Cat2 EPEs

LHRproxy values, strong divergent outflow directly above, and negative baroclinic PV tendencies downstream. On the other hand, the pre-existing positive PV anomaly over Europe is amplified by *in situ* positive baroclinic PV tendencies and moves westward. Both the moist-baroclinic development and the amplification and westward shift of the positive PV anomaly over Europe contribute to the fast downstream propagation of the leading edge of the RWP from D-3 to D-2 (negative quasi-barotropic PV tendencies at D-3 around 75°W and positive tendencies at D-2 around 20°W). The peculiar merging of a developing

RWP with remnants of previous RWPs farther downstream could also be identified in the case considered by Teubler and Riemer (2016), which led to a high-impact weather event over Europe. Finally, from D-2 onwards the RWP amplifies further and propagates eastward subject to baroclinic downstream development that is indicated by the phase-shifted quasi-barotropic (blue contours) and baroclinic (orange contours) PV tendencies amplifying both troughs and ridges.

In contrast to the above evolution, the development of T_u and, even more so, the downstream North Atlantic

FIGURE 14 (a–e) The same as
Figure 12 but for the composite of the 100
representative Cat3 EPEs
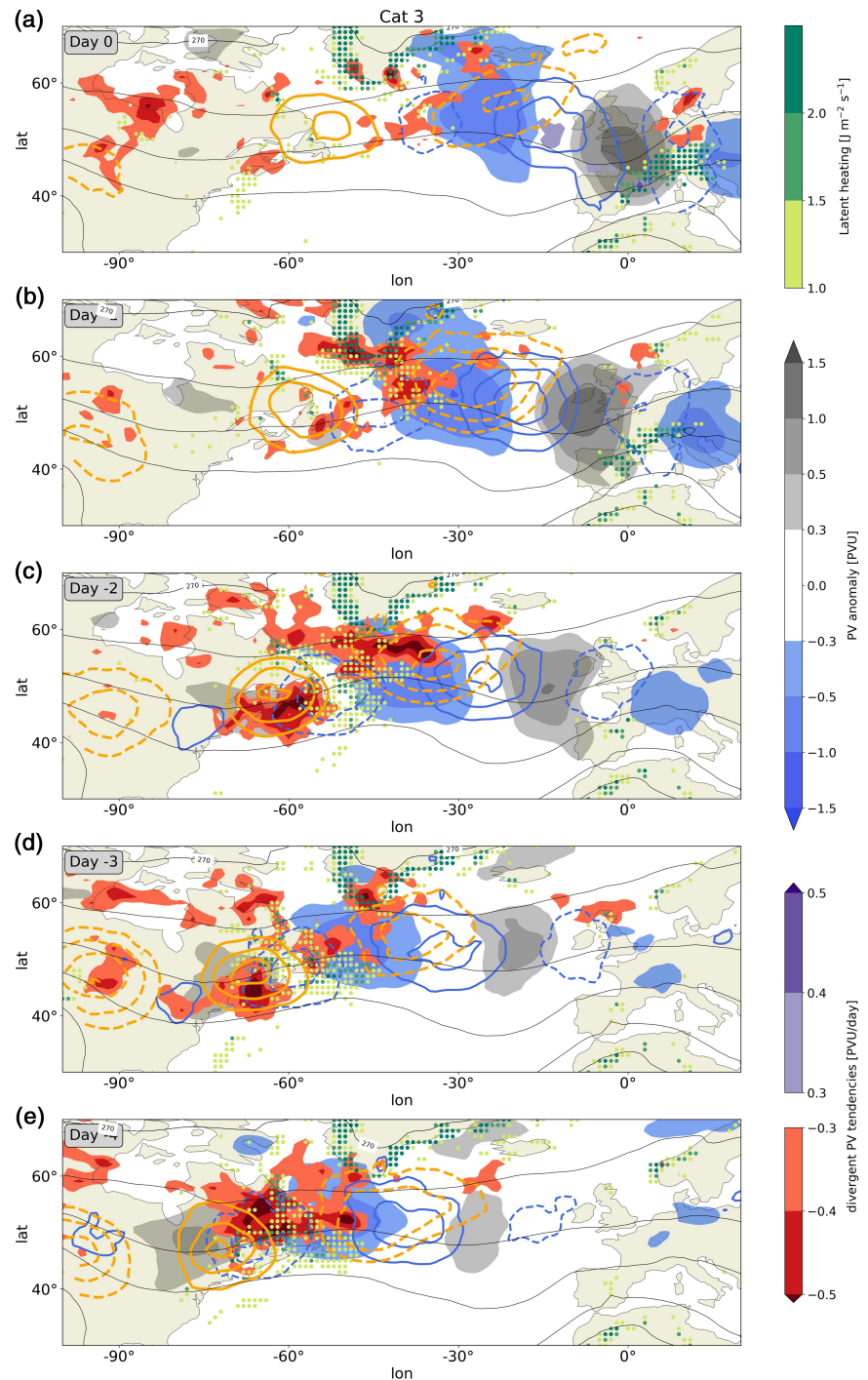
ridge for Cat2 and Cat3 events (Figures 13 and 14) is not
triggered by an incoming RWP but appears to be forced
locally at the North American east coast. As was also evi-
dent in the composite Hovmöller plots (Figure 7), neither
Cat2 nor Cat3 events are associated with a precursor RWP
signal over the North Pacific. At D-4 (Figure 13e), negative
divergent PV tendencies and latent heating (LHRproxy is
even stronger at D-5; not shown) are present in an area
of negative PV anomaly over Newfoundland that falls
in between regions with baroclinic and quasi-barotropic

PV tendencies. At D-3, the negative PV anomaly, the PV
tendencies, and latent heating have all increased dramat-
ically in magnitude, such that a large-amplitude RWP
starts to develop downstream. On this day, the location of
pronounced divergent PV tendency and LHRproxy values
relative to the negative PV anomaly is conducive to a strong
amplification of the ridge. The subsequent RWP propaga-
tion constitutes an archetypical example of downstream
baroclinic development as described above with the ridge
over the North American east coast being the source:

positive quasi-barotropic PV tendencies at the leading edge (around −35°W) form and intensify the trough downstream, while the ridge amplification is maintained by negative baroclinic and divergent PV tendencies. At D-2, a new positive PV anomaly develops at around 15°E reflecting the downstream propagation of the RWP. It is worth noting, that from D-3 onward a consistent and noticeable phase difference between baroclinic and quasi-barotropic tendencies is evident; a configuration that is particularly favourable to strong baroclinic downstream development.

The evolution of Cat3 events is similar to Cat2, but starts earlier and the PV anomaly and tendency fields have a weaker magnitude. The overall slower RWP propagation is associated with the weaker baroclinicity (grey lines) and jets associated with this category (Figures 8 and 11). Concerning the stronger North Atlantic ridge amplification in Cat2 and Cat3 compared to the corresponding Cat1 evolution, it is worth noting that the simultaneous presence of baroclinic interaction and substantial latent heating induces a particularly intense divergent outflow, leading to strong ridge amplification and high-amplitude RWPs. These findings are supported by the Teubler and Riemer (2020) study which showed, in a statistical sense, that both processes are similarly important for ridge building, and that high latent heat release is on average accompanied by strong baroclinic interaction (and vice versa). The strong IVT anomalies observed in the western North Atlantic in the days preceding Cat2 (Figure 11h) and, slightly less so, Cat3 (Figure 11i) events, along with the weaker jet conditions of the corresponding months, may therefore constitute perfect environmental conditions for strong ridge building and further downstream propagation.

5 | CONCLUSIONS

In this study we analysed the linkage between extreme precipitation events (EPEs) over northern-central Italy and the hemispheric evolution leading to the synoptic-scale wave that provides the dynamical forcing and water vapour transport convergence that are necessary for extreme precipitation over this area. We investigated a large number of EPEs that occurred between 1979 and 2015, subdivided into three categories identified in Part I of this study (Cat1, Cat2, Cat3) according to the thermodynamic and dynamic conditions over the target region. The three categories differ not only locally but also in the evolution of the upstream RWP precursor signal. In particular, the key results of this study can be summarized as follows:

- The three EPE categories have a different monthly distribution and are characterized by distinct spatial patterns in precipitation, low-level wind, and moisture transport. These analyses add to the results of Part I and provide further insight into the characteristics of the three categories.

- The probability of heavy precipitation events in northern-central Italy increases with increasing waviness in the upper-tropospheric flow. This clear dependence is found for both Cat1 and Cat2 EPEs. In contrast, the probability of Cat 3 EPEs, which are mostly associated with thermodynamic instability and weakly-forced convection, does not increase with the magnitude of waviness.

- Differences in the evolution and characteristic properties of RWPs for the three EPE categories are evident. These differences are not purely explained by differences in the monthly distribution of the three categories, since they are still evident when restricting the analysis to November cases only.

- A comprehensive PV tendency analysis reveals pronounced differences in the dynamical processes leading to the RWP amplification over the North Atlantic that are crucial for the occurrence of Cat1 and Cat2 EPEs. Cat1 EPEs are characterized by (a) an incoming precursor wave signal from the North Pacific, (b) moist-baroclinic development over the North Atlantic, and (c) an interaction with a pre-existing upper-level positive PV anomaly over Europe. This combination leads to rapid downstream propagation of the leading edge of the RWP. In contrast, Cat2 EPEs arise from RWP amplification along the North American east coast, which is strongly invigorated by divergent outflow associated with latent heat release below. The subsequent downstream propagation is characterized by moist-baroclinic development and favoured by the phase difference between baroclinic and quasi-barotropic tendencies, so that a high-amplitude trough develops over western Europe.

These outcomes suggest that the occurrence of northern-central Italy EPEs depends not only on the local conditions, but also on the large-scale upper-tropospheric flow evolution in the days leading to the events. The particular severity of Cat2 EPEs appears to be the result of favourable conditions in both of these respects, that is, a warmer Mediterranean Sea in autumn and a more vigorous RWP amplification over the North Atlantic.

These results improve our understanding of the synoptic-scale dynamical and thermodynamical processes, providing further evidence on the role and properties of the upstream upper-tropospheric flow leading to EPEs. The processes and mechanisms involved in this regard are not only relevant for a better assessment of

the predictability and impact of these events, but also for their long-term trends. For example, all else being equal, a further increase in water vapour transport in the western North Atlantic, induced by global warming, could induce more frequent or stronger ridge building and downstream development of the kind observed in Cat2 EPEs. Consequently, further studies in this direction appear essential for advancing our knowledge on the occurrence of heavy precipitation events at weather and climate time-scales.

ORCID
Federico Grazzini https://orcid.org/0000-0002-3435-2376

REFERENCES
Barton, Y., Giannakaki, P., von Waldow, H., Chevalier, C., Pfahl, S. and Martius, O. (2016) Clustering of regional-scale extreme precipitation events in southern Switzerland. *Monthly Weather Review*, 144, 347–369. https://doi.org/10.1175/MWR-D-15-0205.1.

Boers, N., Goswami, B., Rheinwalt, A., Bookhagen, B., Hoskins, B.J. and Kurths, J. (2019) Complex networks reveal global pattern of extreme-rainfall teleconnections. *Nature*, 566(7744), 373–377. https://doi.org/10.1038/s41586-018-0872-x.

Branstator, G. (2002) Circumglobal teleconnections, the jet stream waveguide, and the North Atlantic Oscillation. *Journal of Climate*, 15(14), 1893–1910. https://doi.org/10.1175/1520-0442(2002)015h1893:CTTJSWi2.0.CO;2.

Brönnimann, S., Rajczak, J., Fischer, E.M., Raible, C.C., Rohrer, M. and Schär, C. (2018) Changing seasonality of moderate and extreme precipitation events in the Alps. *Natural Hazards and Earth System Sciences*, 18(7), 2047–2056. https://doi.org/10.5194/nhess-18-2047-2018.

Charney, J. (1955) The use of the primitive equations of motion in numerical prediction. *Tellus*, 7, 22–26. https://doi.org/10.3402/tellusa.v7i1.8772.

Davis, C.A. (1992) Piecewise potential vorticity inversion. *Journal of the Atmospheric Sciences*, 49, 1397–1411. https://doi.org/10.1175/1520-0469(1992)049<1397:PPVI>2.0.CO;2.

Dee, D.P., Uppala, S.M., Simmons, A.J., Berrisford, P., Poli, P., Kobayashi, S., Andrae, U., Balmaseda, M.A., Balsamo, G., Bauer, P., Bechtold, P., Beljaars, A.C.M., van de Berg, L., Bidlot, J., Bormann, N., Delsol, C., Dragani, R., Fuentes, M., Geer, A.J., Haimberger, L., Healy, S.B., Hersbach, H., Hólm, E.V., Isaksen, L., Kållberg, P., Köhler, M., Matricardi, M., McNally, A.P., Monge-Sanz, B.M., Morcrette, J.-J., Park, B.-K., Peubey, C., de Rosnay, P., Tavolato, C., Thépaut, J.-N. and Vitart, F. (2011) The ERA-Interim reanalysis: configuration and performance of the data assimilation system. *Quarterly Journal of the Royal Meteorological Society*, 137(656), 553–597. https://doi.org/10.1002/qj.828.

Done, J.M., Craig, G.C., Gray, S.L., Clark, P.A. and Gray, M.E.B. (2006) Mesoscale simulations of organized convection: importance of convective equilibrium. *Quarterly Journal of the Royal Meteorological Society*, 132(616), 737–756. https://doi.org/10.1256/qj.04.84.

Eady, E.T. (1949) Long waves and cyclone waves. *Tellus*, 1A, 33–52. https://doi.org/10.1111/j.2153-3490.1949.tb01265.x.

Fragkoulidis, G., Wirth, V., Bossmann, P. and Fink, A.H. (2018) Linking Northern Hemisphere temperature extremes to Rossby wave packets. *Quarterly Journal of the Royal Meteorological Society*, 144(711), 553–566. https://doi.org/10.1002/qj.3228.

Fragkoulidis, G. and Wirth, V. (2020) Local Rossby wave packet amplitude, phase speed, and group velocity: seasonal variability and their role in temperature extremes. *Journal of Climate*, 33, 8767–8787. https://doi.org/10.1175/JCLI-D-19-0377.1.

Ghinassi, P., Fragkoulidis, G. and Wirth, V. (2018) Local finite-amplitude wave activity as a diagnostic for Rossby wave packets. *Monthly Weather Review*, 146(12), 4099–4114. https://doi.org/10.1175/MWR-D-18-0068.1.

Grams, C. and Archambault, H. (2016) The key role of diabatic outflow in amplifying the midlatitude flow: a representative case study of weather systems surrounding western North Pacific extratropical transition. *Monthly Weather Review*, 144(10), 3847–3869. https://doi.org/10.1175/MWR-D-15-0419.1.

Grams, C., Magnusson, L. and Madonna, E. (2018) An atmospheric dynamics perspective on the amplification and propagation of forecast error in numerical weather prediction models: a case study. *Quarterly Journal of the Royal Meteorological Society*, 144(717), 2577–2591. https://doi.org/10.1002/qj.3353.

Grazzini, F. (2007) Predictability of a large-scale flow conducive to extreme precipitation over the western Alps. *Meteorology and Atmospheric Physics*, 95(3–4), 123–138. https://doi.org/10.1007/s00703-006-0205-8.

Grazzini, F., Craig, G., Keil, C., Antolini, G. and Pavan, V. (2020a) Extreme precipitation events over northern Italy. Part I: A systematic classification with machine-learning techniques. *Quarterly Journal of the Royal Meteorological Society*, 146(726), 69–85. https://doi.org/10.1002/qj.3635.

Grazzini, F., Fragkoulidis, G., Pavan, V. and Antolini, G. (2020b) The 1994 Piedmont flood: an archetype of extreme precipitation events in northern Italy. *Bulletin of Atmospheric Science and Technology*, 1–13. https://doi.org/10.1007/s42865-020-00018-1.

Harris, F.J. (1978) On the use of windows for harmonic analysis with the discrete Fourier transform. *Proceedings of the Institute of Electrical and Electronic Engineers*, 66(1), 51–83.

Hersbach, H., Bell, B., Berrisford, P., Hirahara, S., Horányi, A., Muñoz-Sabater, J., Nicolas, J., Peubey, C., Radu, R., Schepers, D., Simmons, A., Soci, C., Abdalla, S., Abellan, X., Balsamo, G.,

Bechtold, P., Biavati, G., Bidlot, J., Bonavita, M., De Chiara, G., Dahlgren, P., Dee, D., Diamantakis, M., Dragani, R., Flemming, J., Forbes, R., Fuentes, M., Geer, A., Haimberger, L., Healy, S., Hogan, R.J., Hólm, E., Janisková, M., Keeley, S., Laloyaux, P., Lopez, P., Lupu, C., Radnoti, G., de Rosnay, P., Rozum, I., Vamborg, F., Villaume, S. and Thépaut, J.-N. (2020) The ERA5 global reanalysis. *Quarterly Journal of the Royal Meteorological Society*, 146(730), 1999–2049. https://doi.org/10.1002/qj.3803.

Hoskins, B.J. (1975) The geostrophic momentum approximation and the semi-geostrophic equations. *Journal of the Atmospheric Sciences*, 32(2), 233–242. https://doi.org/10.1175/1520-0469(1975)032%3C0233:TGMAAT%3E2.0.CO;2.

Hoskins, B.J., McIntyre, M.E. and Robertson, A.W. (1985) On the use and significance of isentropic potential vorticity maps. *Quarterly Journal of the Royal Meteorological Society*, 111(470), 877–946. https://doi.org/10.1002/qj.49711147002.

Hoskins, B.J. and Ambrizzi, T. (1993) Rossby wave propagation on a realistic longitudinally varying flow. *Journal of the Atmospheric Sciences*, 50(12), 1661–1671. https://doi.org/10.1175/1520-0469(1993)050<1661:RWPOAR>2.0.CO;2.

Isotta, F., Frei, C., Weilguni, V., Percec Tadic, M., Lassègues, P., Rudolf, B., Pavan, V., Cacciamani, C., Antolini, G., Ratto, S.M., Munari, M., Micheletti, S., Bonati, V., Lussana, C., Ronchi, C., Panettieri, E., Marigo, G. and Vartacnik, G. (2014) The climate of daily precipitation in the Alps: development and analysis of a high-resolution grid dataset from pan-Alpine rain-gauge data. *International Journal of Climatology*, 34, 1657–1675. https://doi.org/10.1002/joc.3794.

Liu, B., Tan, X., Gan, T.Y., Chen, X., Lin, K., Lu, M. and Liu, Z. (2020) Global atmospheric moisture transport associated with precipitation extremes: mechanisms and climate change impacts. *WIREs Water*, 7. https://doi.org/10.1002/wat2.1412.

Loriaux, J.M., Lenderink, G. and Siebesma, A.P. (2017) Large-scale controls on extreme precipitation. *Journal of Climate*, 30, 955–968. https://doi.org/10.1175/JCLI-D-16-0381.1.

Manola, I., Selten, F., de Vries, H. and Hazeleger, W. (2013) "Waveguidability" of idealized jets. *Journal of Geophysical Research: Atmospheres*, 118, 10432–10440. https://doi.org/10.1002/jgrd.50758.

Martius, O., Schwierz, C. and Davies, H.C. (2006b) A refined Hovmöller diagram. *Tellus A*, 58(2), 221–226. https://doi.org/10.1111/j.1600-0870.2006.00172.x.

Martius, O., Schwierz, C. and Davies, H.C. (2008) Far-upstream precursors of heavy precipitation events on the Alpine south-side. *Quarterly Journal of the Royal Meteorological Society*, 134(631), 417–428. https://doi.org/10.1002/qj.229.

Martius, O., Zenklusen, E., Schwierz, C. and Davies, H.C. (2006a) Episodes of Alpine heavy precipitation with an overlying elongated stratospheric intrusion: a climatology. *International Journal of Climatology*, 26(9), 1149–1164. https://doi.org/10.1002/joc.1295.

Moore, B.J., Keyser, D. and Bosart, L.F. (2019) Linkages between extreme precipitation events in the central and eastern United States and Rossby wave breaking. *Monthly Weather Review*, 147(9), 3327–3349. https://doi.org/10.1175/MWR-D-19-0047.1.

Pasquier, J.T., Pfahl, S. and Grams, C.M. (2019) Modulation of atmospheric river occurrence and associated precipitation extremes in the North Atlantic region by European weather regimes. *Geophysical Research Letters*, 46, 1014–1023. https://doi.org/10.1029/2018GL08119.

Pavan, V., Antolini, G., Barbiero, R., Berni, N., Brunier, F., Cacciamani, C., Cagnati, A., Cazzuli, O., Cicogna, A., De Luigi, C., Di Carlo, E., Francioni, M., Maraldo, L., Marigo, G., Micheletti, S., Onorato, L., Panettieri, E., Pellegrini, U., Pelosini, R., Piccinini, D., Ratto, S., Ronchi, C., Rusca, L., Sofia, S., Stelluti, M., Tomozeiu, R. and Malaspina, T.T. (2019) High resolution climate precipitation analysis for north-central Italy, 1961–2015. *Climate Dynamics*, 52(5–6), 3435–3453. https://doi.org/10.1007/s00382-018-4337-6.

Persson, A. (2017) The story of the Hovmöller diagram: an (almost) eyewitness account. *Bulletin of the American Meteorological Society*, 98(5), 949–957. https://doi.org/10.1175/BAMS-D-15-00234.1.

Petrucci, O., Aceto, L., Bianchi, C., Bigot, V., Brázdil, R., Pereira, S., Kahraman, A., Kiliç, Ö., Kotroni, V., Llasat, M.C., Llasat-Botija, M., Papagiannaki, K., Pasqua, A.A., Řehoř, J., Geli, J.R., Salvati, P., Vinet, F. and Zêzere, J.L. (2019) Flood fatalities in Europe, 1980–2018: variability, features, and lessons to learn. *Water*, 11(8), 1682. https://doi.org/10.3390/w11081682.

Piaget, N., Froidevaux, P., Giannakaki, P., Gierth, F., Martius, O., Riemer, M., Wolf, G. and Grams, C.M. (2015) Dynamics of a local Alpine flooding event in October 2011: moisture source and large-scale circulation. *Quarterly Journal of the Royal Meteorological Society*, 141(690), 1922–1937. https://doi.org/10.1002/qj.2496.

Pinto, J., Ulbrich, S., Parodi, A., Rudari, R., Boni, G. and Ulbrich, U. (2013) Identification and ranking of extraordinary rainfall events over northwest Italy: the role of Atlantic moisture. *Journal of Geophysical Research: Atmospheres*, 118, 2085–2097. https://doi.org/10.1002/jgrd.50179.

Pohorsky, R., Röthlisberger, M., Grams, C., Riboldi, J. and Martius, O. (2019) The climatological impact of recurring North Atlantic tropical cyclones on downstream extreme precipitation events. *Monthly Weather Review*, 147(5), 1513–1532. https://doi.org/10.1175/MWR-D-18-0195.1.

Röthlisberger, M., Frossard, L., Bosart, L.F., Keyser, D. and Martius, O. (2019) Recurrent synoptic-scale Rossby wave patterns and their effect on the persistence of cold and hot spells. *Journal of Climate*, 32(11), 3207–3226. https://doi.org/10.1175/JCLI-D-18-0664.1.

Rousseeuw, P.J. (1987) Silhouettes: a graphical aid to the interpretation and validation of cluster analysis. *Computational and Applied Mathematics*, 20, 53–65. https://doi.org/10.1016/0377-0427(87)90125-7.

Scoccimarro, E., Gualdi, S. and Krichak, S. (2018) Extreme precipitation events over north-western Europe: getting water from the tropics. *Annals of Geophysics*, 61(4). https://doi.org/10.4401/ag-7772.

Snyder, C., Skamarock, W.C. and Rotunno, R. (1991) A comparison of primitive-equation and semigeostrophic simulations of baroclinic waves. *Journal of the Atmospheric Sciences*, 48(19), 2179–2194. https://doi.org/10.1175/1520-0469(1991)048%3C2179:ACOPEA%3E2.0.CO;2.

Sodemann, H. and Zubler, E. (2010) Seasonal and inter-annual variability of the moisture sources for Alpine precipitation during 1995-2002. *International Journal of Climatology*, 30(7), 947–961. https://doi.org/10.1002/joc.1932.

Teubler, F. and Riemer, M. (2016) Dynamics of Rossby wave packets in a quantitative potential vorticity–potential temperature framework. *Journal of the Atmospheric Sciences*, 73(3), 1063–1081. https://doi.org/10.1175/JAS-D-15-0162.1.

Teubler, F. and Riemer, M. (2020) Potential-vorticity dynamics of troughs and ridges within Rossby wave packets during a 40-year reanalysis period. *Weather and Climate Dynamics*. https://doi.org/10.5194/wcd-2020-52.

Trenberth, K.E. and Solomon, A. (1994) The global heat balance: heat transports in the atmosphere and ocean. *Climate Dynamics*, 10, 107–134.

Wernli, B. and Davies, H. (1997) A Lagrangian-based analysis of extratropical cyclones. I: The method and some applications. *Quarterly Journal of the Royal Meteorological Society*, 123(538), 467–489. https://doi.org/10.1002/qj.49712353811.

Winschall, A., Sodemann, H., Pfahl, S. and Wernli, H. (2014) How important is intensified evaporation for Mediterranean precipitation extremes? *Journal of Geophysical Research: Atmospheres*, 119(9), 5240–5256. https://doi.org/10.1002/2013JD021175.

Wirth, V., Riemer, M., Chang, E.K. and Martius, O. (2018) Rossby wave packets on the midlatitude waveguide: a review. *Monthly Weather Review*, 146(7), 1965–2001. https://doi.org/10.1175/MWR-D-16-0483.1.

Wirth, V. (2020) Waveguidability of idealized midlatitude jets and the limitations of ray tracing theory. *Weather and Climate Dynamics*, 1, 111–125. https://doi.org/10.5194/wcd-1-111-2020.

Zimin, A.V., Szunyogh, I., Patil, D.J., Hunt, B.R. and Ott, E. (2003) Extracting envelopes of Rossby wave packets. *Monthly Weather Review*, 131(5), 1011–1017. https://doi.org/10.1175/1520-0493(2003)131h1011:EEORWPi2.0.CO;2.

Zimmer, M., Craig, G.C., Keil, C. and Wernli, H. (2011) Classification of precipitation events with a convective response timescale and their forecasting characteristics. *Geophysical Research Letters*, 38, L05802. https://doi.org/10.1029/2010GL046199.